Hu *et al. Microstructures* **2025**, *5*, 2025082
DOI: 10.20517/microstructures.2024.184

Microstructures

Review

Open Access

Check for updates

Photonic meta-crystals

Shengyu Hu[#], Pengyu Li[#], Hong Chen, Zhiwei Guo

Key Laboratory of Advanced Micro-structure Materials, MOE, School of Physics Science and Engineering, Tongji University, Shanghai 200092, China.
[#]Authors contributed equally.

Correspondence to: Prof. Zhiwei Guo, Key Laboratory of Advanced Micro-structure Materials, MOE, School of Physics Science and Engineering, Tongji University, 1239 Siping Road, Yangpu district, Shanghai 200092, China. E-mail: 2014guozhiwei@tongji.edu.cn

How to cite this article: Hu, S.; Li, P.; Chen, H.; Guo, Z. Photonic meta-crystals. *Microstructures* **2025**, *5*, 2025082. https://dx.doi.org/10.20517/microstructures.2024.184

Received: 27 Dec 2024 **First Decision:** 26 Mar 2025 **Revised:** 9 May 2025 **Accepted:** 4 Jun 2025 **Published:** 8 Jul 2025

Academic Editor: Shujun Zhang **Copy Editor:** Shu-Yuan Duan **Production Editor:** Shu-Yuan Duan

Abstract

Photonic crystals (PCs) and metamaterials are periodic artificial structures with different scales that modulate light–matter interactions. Considering their complementary advantages, the concept of photonic meta-crystals is proposed. In these hybrid structures, such as hypercrystals (composed of hyperbolic metamaterials and PCs), the photonic band gap provided by PCs can be blue-shifted with more degrees of freedom, and the weak coupling of hyperbolic metamaterials to the environment can be enhanced. This review introduces photonic meta-crystals in sequence, based on the classification of electromagnetic parameters in metamaterials. Recent advances in photonic meta-crystals are also presented in the context of topological semimetals.

Keywords: Metamaterials, effective medium theory, photonic crystals, light-matter interactions, microstructures

INTRODUCTION

In electronic systems, the interactions between electrons and atoms in practical materials seem elusive due to the enormous magnitude near 10^{23} cm^{-3}. Nevertheless, approximations like the Born-Oppenheimer adiabatic approximation, Hatree-Fock mean-field theory, and periodic potential theory provide an elegant way to simplify the problem into the motion of a single electron in an effective periodic potential, which led to the concept of energy bands established by F. Bloch in 1928[1]. More specifically, the periodic potential tends to originate from the regular arrangement of atoms with discrete spatial translation symmetry,

corresponding to crystalline lattices in metals and semiconductors. The great success of energy band theory has motivated significant developments in the microelectronics industry and inspired further exploration into extensive fields, such as photonic counterparts. Compared with electrons, photons exhibit several characteristics fulfilling the first two approximations: on the one hand, they have no mass and travel at the highest velocity; on the other hand, they do not interact with each other. By introducing periodic potentials through alternating dielectric layers, the concept of the photonic crystal (PC) was independently proposed by Yablonovitch[2] and John[3] in 1987. When the lattice constant is comparable to the wavelength of light, multiple Bragg scattering mechanisms can inhibit spontaneous emission and support photon localization within the photonic band gap. Due to their characteristics, photons inherently avoid redundant energy consumption caused by Joule heating, making them well-suited for use in integrated and miniaturized devices. However, the flexible modulation of photons remains challenging due to the absence of photon-photon interactions. The photonic band gap in PCs provides a direct method to control photons, leading to various applications in recent years, including fibers[4-8], lasers[9,10], signal processing[11-13], and image differentiation[14-17].

For the periodic structure, when reducing the lattice constant to a subwavelength scale, the dominant Mie scattering gives rise to optically induced electric or magnetic resonances based on displacement currents[18,19], leading to the opening of a Mie band gap below the lowest Bragg band gap[20]. Under these conditions, the entire structure can be effectively treated as a homogeneous medium according to effective medium theory (EMT). Here, the electromagnetic field components are regarded as continuous and constant within each layer, complying with the boundary conditions derived from Maxwell's equations[21]. Intriguingly, these artificially designed structures, known as metamaterials[22], exhibit distinct electromagnetic responses that surpass those of conventional dielectrics, which typically possess positive permittivity $\varepsilon > 0$ and permeability $\mu > 0$. Through meticulous and rational design, metamaterials can realize counterintuitive phenomena previously deemed impossible, such as electromagnetic cloaking[23-25], negative refraction[26-28], and superlensing[29-31].

Although PCs and metamaterials each possess distinctive advantages, their individual limitations restrict comprehensive control over light. PCs effectively create band gaps through Bragg scattering; however, they are constrained by blue shift dispersion under oblique incidence and lack flexibility in engineering arbitrary electromagnetic parameters. On the other hand, metamaterials enable unconventional optical phenomena like negative refraction but frequently encounter challenges related to narrow operational bandwidths and significant energy dissipation. Recent advancements in photonic meta-crystals (PMCs), formed by integrating PCs and metamaterials (as illustrated in Figure 1), have opened new avenues for manipulating light. By combining the broadband dispersion control capabilities of PCs with the customized electromagnetic properties of metamaterials, PMCs overcome critical limitations inherent to each individual technology. Specifically, these hybrid systems compensate for spectral shifts resulting from Bragg scattering through the use of hyperbolic metamaterials[32], enhance light-matter interactions via zero-index materials[33,34], and alleviate the narrow bandwidth[35] and intrinsic losses typical of conventional metamaterials. This synergistic integration facilitates innovative functionalities, including nonreciprocal transport[36] and topological protection[37], which will be extensively discussed throughout this review. In the first part of this review, we explore the physical properties of PMCs arising from the integration of various classes of metamaterials. Under transverse magnetic (TM) excitation, these metamaterials can be broadly categorized by their effective permittivity and permeability. The integration of these metamaterials into PCs can yield diverse optical behaviors depending on their electromagnetic characteristics and structural configurations. One representative category is left-handed materials (LHM), characterized by simultaneously $\varepsilon < 0$ and $\mu < 0$. When integrated into photonic crystals, they can produce omnidirectional

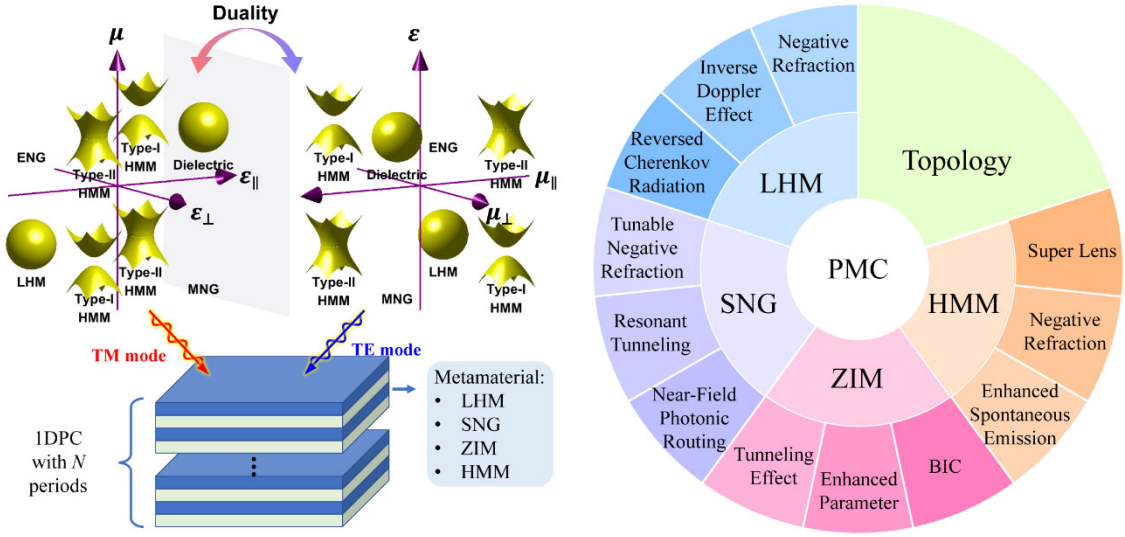

Figure 1. The family of metamaterials and a schematic illustration of photonic meta-crystals. The diagram on the right presents a structural roadmap depicting the integration process and functional evolution of these metamaterials within photonic meta-crystals. LHM: Left-handed material; SNG: single-negative; ZIM: zero-index material; HMM: hyperbolic metamaterial; PMC: photonic meta-crystal.

photonic band gaps that are insensitive to the angle of incidence, owing to the zero average refractive index condition[38]. Such structures also support negative refraction[26-28], superlensing[39,40], and reversed Doppler and Cherenkov effects[41-47]. Single-negative (SNG) materials, which exhibit either $\varepsilon < 0$, $\mu > 0$ or $\varepsilon > 0$, $\mu < 0$, provide further means to manipulate reflection phase and band topology when integrated into photonic crystal structures. Pairings of epsilon-negative (ENG) and mu-negative (MNG) materials can support resonant tunneling and complete transmission when phase and impedance are properly matched[48]. In addition, asymmetric designs enable flexible control of dispersion and near-field tuning[49-51]. Zero-index materials (ZIMs), characterized by $\varepsilon = 0$ and/or $\mu = 0$, support nearly uniform phase propagation and enable wave tunneling through structures of arbitrary geometry[52-55]. Their strong field enhancement benefits nonlinear processes[31,57,77], and supports cloaking[58], photonic doping[59,60], and analog optical computing[61]. Hyperbolic metamaterials (HMMs) exhibit anisotropic permittivity tensors, where type-I satisfy $\varepsilon_\perp < 0$, $\varepsilon_\parallel > 0$, $\mu > 0$, and type-II satisfy $\varepsilon_\perp > 0$, $\varepsilon_\parallel < 0$, $\mu > 0$. These media support high-k modes and broadband dispersion control. When combined with photonic crystals, they can counteract Bragg-induced blue shifts and enhance spontaneous emission[29,32], enable broadband negative refraction[38,62], and produce flat bands or hyperlensing effects in hypercrystals[27,29]. These hybrid mechanisms give PMCs capabilities that neither PCs nor metamaterials can achieve on their own, introducing new degrees of freedom in band structure engineering. Due to electromagnetic duality, similar effects can also be expected under transverse electric (TE) excitation. In the second part of this review, we focus on how PMCs are applied to realize topological and non-Hermitian physics.

PMC WITH LHM

In 1968, V. G.Veselago proposed a peculiar material with $\varepsilon < 0$ and $\mu < 0$, and predicted several fantastic phenomena, including negative refraction, the inverse Doppler effect, and the reversed Cherenkov radiation[63]. In this case, the electric field $\boldsymbol{E}$, the magnetic field $\boldsymbol{H}$, and the wave vector $\boldsymbol{k}$ form a left-handed set, corresponding to a negative index $n = -\sqrt{\varepsilon \cdot \mu} < 0$. In 2001, Shelby *et al.* designed a composite structure, as shown in Figure 2A, to realize the proposed concept. The periodic wire array exhibits plasmon resonance with $\varepsilon < 0$, and the split-ring resonators exhibit magnetic resonance with $\mu < 0$[36]. This breakthrough marked

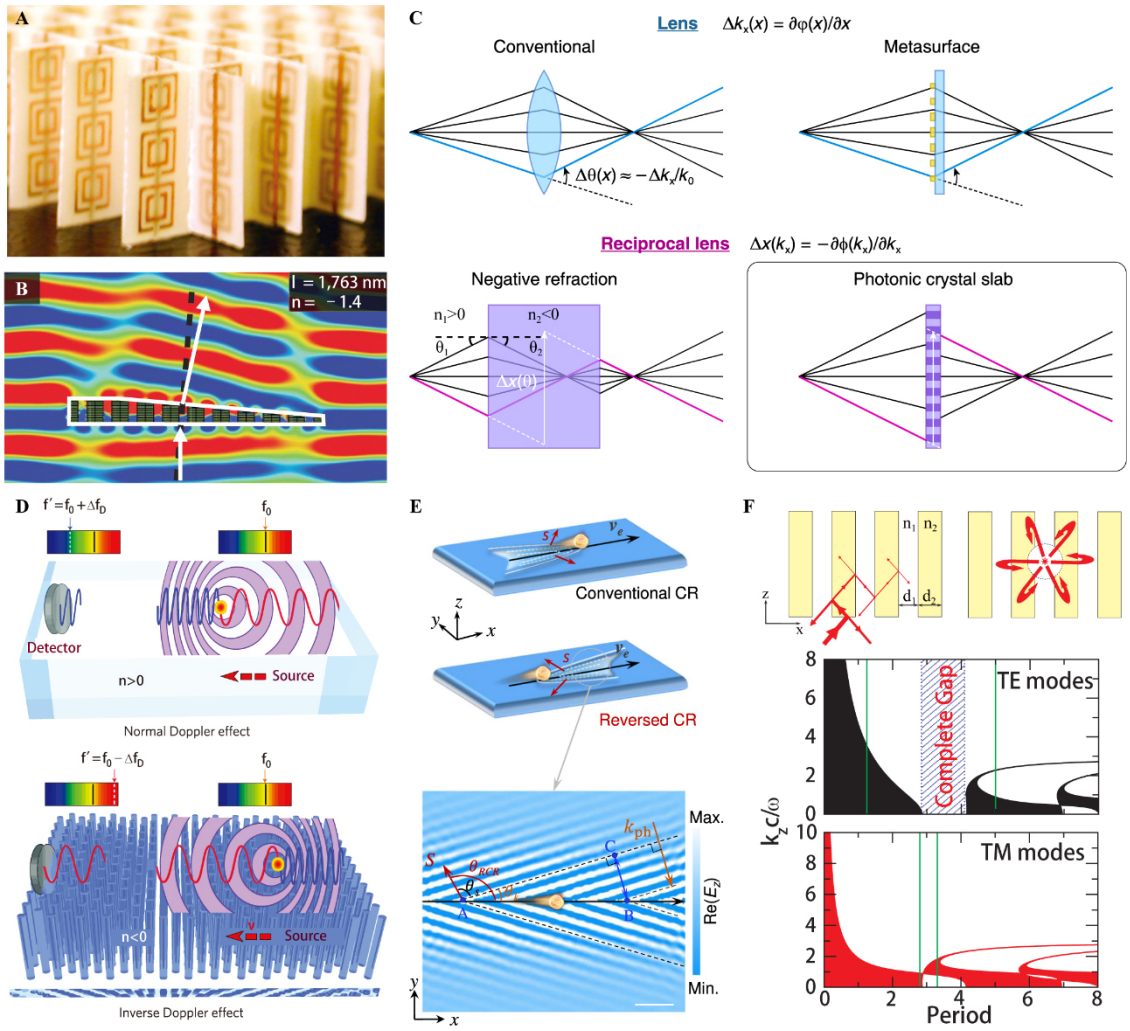

Figure 2. (A) Photograph of the left-handed metamaterial (LHM), quoted with permission from Shelby *et al.*[26]; (B) The phase front of the light shows the negative refraction angle, quoted with permission from Valentine *et al.*[27]; (C) Comparison between the conventional lens, metasurfaces lens, and two superlenses with negative refraction and photonic crystal slab, quoted with permission from Liu *et al.*[40]; (D) Schematic showing the normal Doppler effect in normal materials ($n > 0$) and inverse Doppler effect in LHM ($n < 0$), quoted with permission from Chen *et al.*[43]; (E) Schematic representation of conventional and reversed Cherenkov radiation (CR) excited via a moving charge, quoted with permission from Guo *et al.*[47]; (F) Schematic of the PC containing LHM with the ray diagram for the end-fire wave propagation and suppression of radiation of a local source placed inside, quoted with permission from Shadrivov *et al.*[64].

the beginning of a new era in metamaterials, allowing researchers to explore physical properties beyond those found in natural materials. Subsequently, the predicted phenomena were experimentally demonstrated, including:

The negative refraction[36-40]

As shown in Figure 2B, when light passes through the surface, the incident ray in medium 1 with refractive index $n_1 > 0$ and the refracted ray in medium 2 with index $n_2 < 0$ appear on the same side of the normal line, following Snell's law $n_1 \sin\theta_1 = n_2 \sin\theta_2$. Under this condition, a simple parallel-sided LHM slab can act as a superlens with double focusing, transverse invariance, and aberration-free performance in principle[39]. However, this design relies on the slab being thick enough to support a propagation phase, and fabricating a bulky LHM is difficult. Although negative refraction has been well demonstrated at microwave frequencies,

its realization in the optical range faces major challenges, mainly due to high ohmic losses in metals and the difficulty of scaling structures such as split-ring resonators to deep-subwavelength dimensions. In addition, achieving isotropic and broadband negative index responses requires careful suppression of anisotropy and parasitic coupling. To overcome these limitations, researchers have explored alternative strategies including dielectric resonators, planar metamaterials, and metasurfaces that mimic left-handed behavior with improved scalability and reduced loss. Notably, Liu *et al.* propose a reciprocal lens based on the PC slab, as shown in Figure 2C, where the ray can be laterally shifted by modulating the phase in momentum space[40].

The inverse Doppler effect[41-43]

When a source with the frequency ω_0 moves away from the receiver at velocity v, the received frequency becomes $\omega = \omega_0(1+\frac{v}{u})$, showing a blue shift that increases with v, where u is the velocity of energy flow. This effect is shown in Figure 2D and suggests potential applications in tunable and multi-frequency radiation sources.

The reversed Cherenkov radiation[44-47]

When fast-moving charged particles with the velocity v bombard the LHM, the direction of coherent radiation is reversed, with the Cherenkov angle θ satisfying $\cos\theta = \frac{c}{nv}$. This backward emission is easily distinguishable from the emitting particles, making it highly valuable for particle detection. The significant advancements in metamaterials have also inspired similar investigations into naturally occurring materials. For instance, van der Waals materials that support hyperbolic phonon polaritons are emerging as promising candidates for applications in the mid-infrared region, as illustrated in Figure 2E[47].

Considering a one-dimensional PC composed of two alternating layers of LHM ($n_A < 0$) and conventional dielectrics ($n_B > 0$), the propagation of electromagnetic waves through such structures can be mathematically described by the transfer matrix method. The characteristic matrix of the j th layer is given by:

$$M_j = \begin{bmatrix} \cos(k_j d_j) & i\eta_j \sin(k_j d_j) \\ i\eta_j^{-1} \sin(k_j d_j) & \cos(k_j d_j) \end{bmatrix} \quad (1)$$

where $k_j = n_j\omega/c$ and $\eta_j = \sqrt{\mu_j / \varepsilon_j}$. This method provides the theoretical foundation for analyzing the unique bandgap characteristics of PMC. In particular, an omnidirectional gap appears when the zero average refractive index condition 12345 is satisfied. Unlike the conventional Bragg gap, this bandgap remains robust against variations in incident angle and polarization, due to the sign reversal of n_A in LHMs[35]. Furthermore, a similar structure with three alternating layers can suppress the Brewster angle condition, enabling the formation of a complete bandgap in all three spatial dimensions, as demonstrated in Figure 2F[64].

PMC WITH SNG MATERIALS

SNG materials can be categorized into ENG, (with $\varepsilon < 0$, $\mu > 0$) and MNG, (with $\varepsilon > 0$, $\mu < 0$). As discussed in the previous section, an isolated SNG layer can, to some extent, serve as an intermediate step or simplified substitute for LHMs. Take the LHM design[36] as an example, the MNG split-ring resonators are placed at the nodes of the magnetic field generated by the ENG wire array, in order to minimize their near-field coupling. Under this configuration, the EMT remains applicable[65]. Moreover, complementary SNG media can replace the LHM-based cloaking shell[66], and two parallel ENG slab waveguides under TM excitation can serve as an alternative to the LHM-based configuration excited by natural light, effectively enhancing optical gradient forces, as shown in Figure 3A[49]. The engineered configurations of SNG materials open new dimensions in photonic control beyond conventional dielectric structures, and their extraordinary

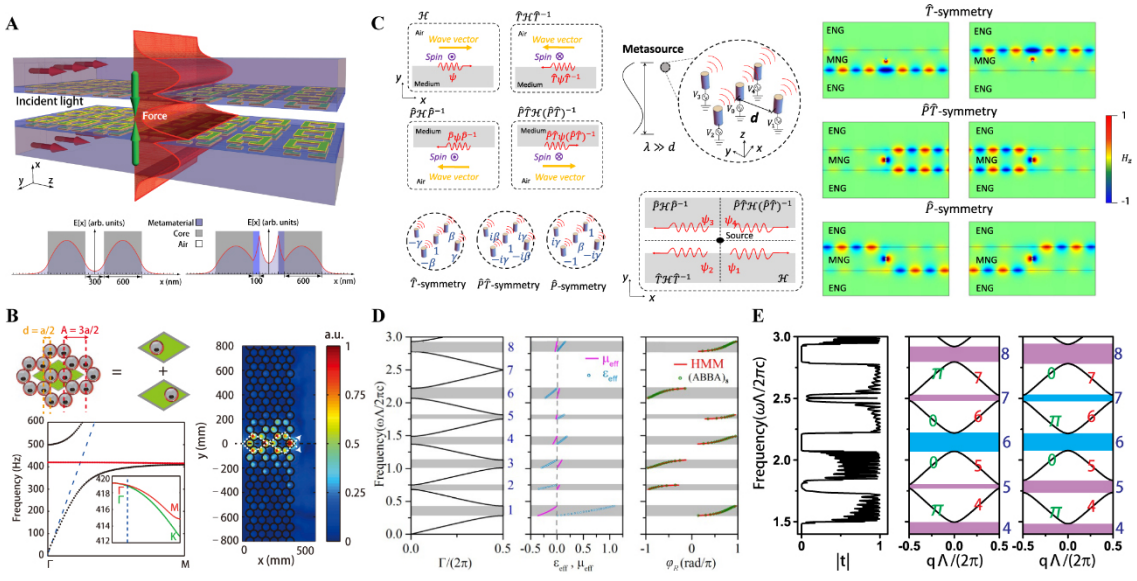

Figure 3. (A) A metamaterial slab that amplifies the evanescent tails to enhance the optical gradient force, quoted with permission from Ginis *et al.*[49]; (B) The bi-periodic honeycomb array with a negative index band (the red line in the lower left panel) and the subwavelength focusing of a super lens, quoted with permission from Kaina *et al.*[50]; (C) The symmetry features in the near-field wave systems and the metasources to demonstrate the near-field photonic routing based on the interface mode between ENG and MNG metamaterials, quoted with permission from Long *et al.*[51]; (D) The band structure, effective parameters (ε and μ), and reflection phase φ_R of the infinite-periodic PC $(ABBA)_N$, quoted with permission from Shi *et al.*[67]; (E) The transmission spectrum of a system composed of PC1 on the left-hand side and PC2 on the right-hand side (the left panel), the band structure (solid black curve) and Zak phase (labeled in green) of PC1 (the middle panel) and PC2 (the right panel), quoted with permission from Xiao *et al.*[68]. ENG: Epsilon-negative; MNG: mu-negative; PC: photonic crystal.

manifestations can be observed through the following aspects:

Tunable negative refraction

When the symmetry of the SNG PC lattice is broken, multiple scattering leads to folding of the lower polariton band in the first Brillouin zone, and opens a narrow transparency window with negative-index dispersion, as shown in Figure 3B[50]. This effect enables super-resolution imaging, high-Q filtering, and enhanced nonlinear optics. When implemented on silicon or III-V platforms, it provides a compact alternative to conventional metamaterials with precise dispersion control.

Resonant tunneling and transparency

Although the isolated ENG or MNG material is opaque, the situation may be different in the heterostructure composed of a lossless ENG-MNG pair. When the matching condition of the impedance $X_1 = -X_2$ and the effective-phase $\beta_1 d_1 = \beta_2 d_2$ is fulfilled, the resonance amplifies the evanescent wave and leads to complete tunneling with high transparency[48]. Here, $X_i = \sqrt{\mu_i / \varepsilon_i}$, β_i, and d_i represent the impedance, wave number, and thickness in the ENG and MNG materials, respectively. The matched pair exhibits angle-selective transparency and localized field enhancement at the interface. Remarkably, the zero-φ_{eff} gap, characterized by scale invariance and robustness against disorder, enables compact photonic devices such as multichannel filters and subwavelength resonators. This performance surpasses that of conventional Bragg-gap-based designs[48]. Although the zero-φ_{eff} gap provides inherent robustness against structural disorder and scale variation, the experimental realization of ENG-MNG tunneling systems still requires careful parameter control to fully utilize these advantages. In particular, achieving the impedance and phase matching condition relies on the precise fabrication of layer thicknesses and consistent material parameters across the interface. Deviations, although sometimes tolerated by the topological features of the structure, may reduce

tunneling efficiency or distort the transparency window. To address these challenges, experimental efforts have adopted techniques such as dielectric doping, impedance inversion calibration, and subwavelength multilayer deposition, which enable the realization of more reproducible and tunable SNG-based meta-crystals for integrated photonic applications.

Near-field photonic routing

Near-field photonic routing utilizes the interface between ENG and MNG metamaterials to control electromagnetic waves at subwavelength scales. By designing metasources with parity ($\hat{P}:\boldsymbol{r}\to-\boldsymbol{r}$), time-reversal ($\hat{T}:t\to-t$), or parity-time ($\hat{P}\hat{T}:\boldsymbol{r}\to-\boldsymbol{r},t\to-t$) symmetry, this method enables precise manipulation of wave propagation. Parity symmetry maintains field distribution under inversion for balanced signal splitting, while breaking time-reversal symmetry enables nonreciprocal routing. Parity-time symmetry creates exceptional points for unidirectional transmission and enhanced sensitivity. These mechanisms make it possible to realize compact photonic circuits with reduced crosstalk, nonreciprocal isolators, and improved near-field sensing. When integrated with PC, the system provides additional control over wave confinement and dispersion, offering new possibilities for advanced photonic devices, as demonstrated in Figure 3C[51].

Intriguingly, the band gaps in PC can be analogous to SNG materials; hence, an interface mode like the Tamm state can form at the boundary when joining two PCs with band gaps of the same frequency but different components[67]. Specifically, the component can be defined by the reflection phase φ_R of the reflection coefficient $r_R = e^{i\varphi_R}$ of the entire PC, as shown in Figure 3D. For the TM polarization, $\varphi_R \in [-\pi, 0]$ denotes the MNG gap, and $\varphi_R \in [0, \pi]$ denotes the ENG gap; for the TE polarization, $\varphi_R \in [-\pi, 0]$ denotes the ENG gap, and $\varphi_R \in [0, \pi]$ denotes the MNG gap[67]. The matching condition is converted to $\varphi_{R1} + \varphi_{R2} = 2m\pi$ ($m \in \mathbb{N}$) at this moment[68]. In the language of topology, the gap can be described by the Zak phase based on the sign of $1\text{-}\varepsilon_1\mu_2/(\varepsilon_2\mu_1)$. The existence of an interface mode is then determined by the sum of all Zak phases below the gap on both sides of the interface, as shown in Figure 3E[68], and is protected against disorder under the condition of zero average effective mass[67].

PMC WITH ZIM

As a transitional category between conventional matters and SNG/NIM, the family of ZIMs can be classified into epsilon-near-zero (ENZ, with $\varepsilon \approx 0$, $\mu \neq 0$), mu-near-zero (MNZ, with $\varepsilon \neq 0$, $\mu \approx 0$), and epsilon-and-mu-near-zero (EMNZ, with $\varepsilon \approx 0$, $\mu \approx 0$), as is shown in Figure 4A[33]. Conveniently, ZIMs can be found near the resonant frequency of the electric and/or magnetic dipole mode, like ENZ in a bulk metal near the plasma frequency, as shown in Figure 4B. However, metal tends to possess significant intrinsic ohmic losses, which leads to short propagation length. To alleviate the impact of ohmic losses, novel natural materials such as two-dimensional (2D) materials are being explored[34]. Two artificial structures are mainly adopted: (1) In a rectangular waveguide with width w, the effective relative permittivity $\varepsilon_{eff}/\varepsilon_0 = n^2 - c^2/(4f^2w^2)$ satisfies the condition of ENZ at the cutoff frequency $f = c/(2w)$[69]. (2) In the PC with a square lattice, the band structure manifests dispersion of a Dirac cone with the pseudospin-1 triply degenerate point, where an electrical monopole mode and a transverse magnetic dipole mode dominate the properties of EMNZ, as shown in Figure 4C[36,52]. When breaking the C_{4v} and time-reversal symmetry by introducing an elliptical cylinder and applying an external magnetic field, the dispersion evolves into pseudospin-1/2 doubly degenerate, and the determinant (instead of the value) of the effective permeability keeps zero[70]. In addition, the out-of-plane radiation loss of PC is further eliminated based on the destructive interference of the bound state in the continuum (BIC)[71]. The various experiment realizations of ZIMs provide powerful platforms to explore and demonstrate the novel features, and several examples are listed below:

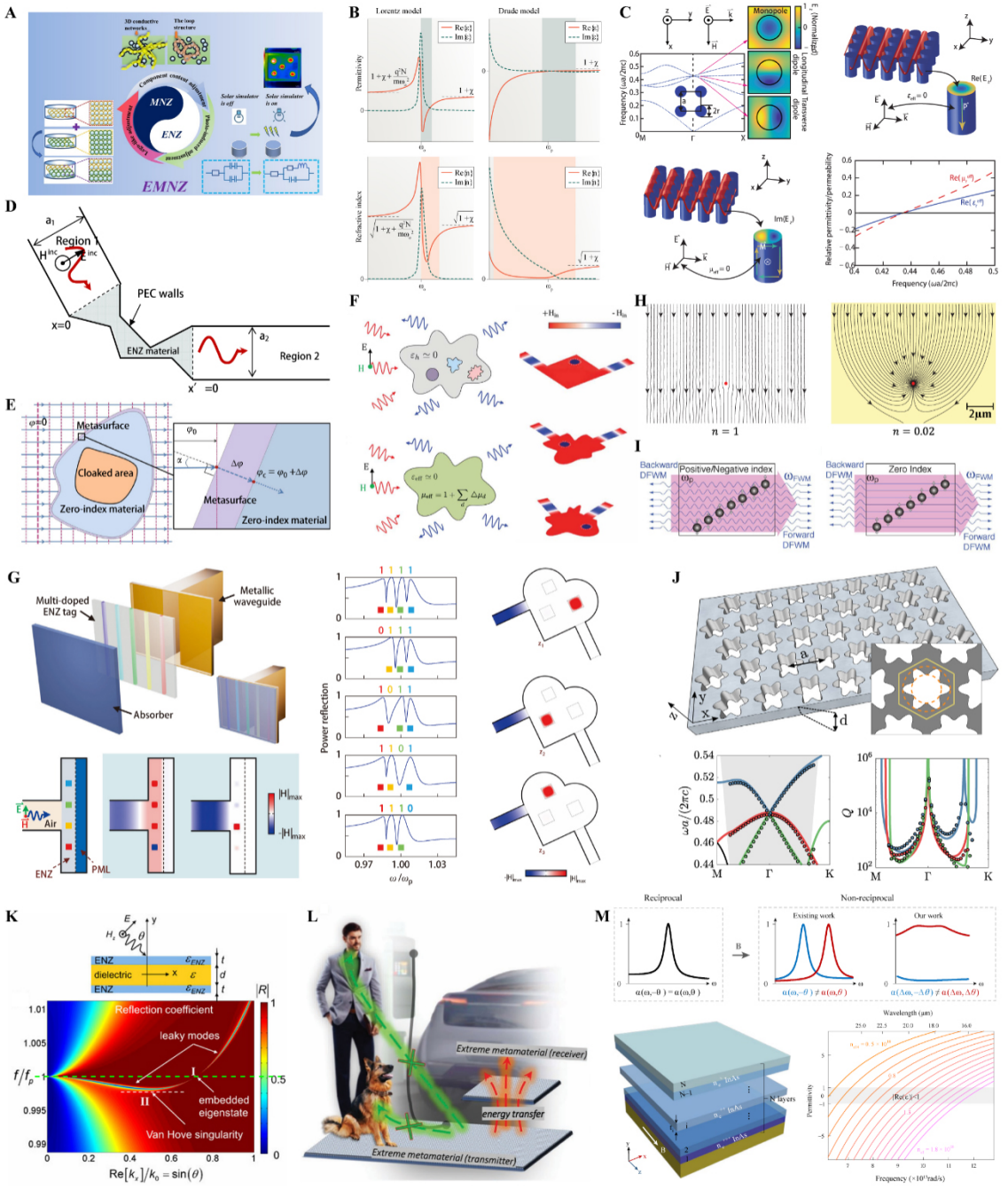

Figure 4. (A) Schematic illustration of the adjustability of EMNZ properties, quoted with permission from Dai *et al.*[33]; (B) The Lorentz model and Drude model of the ENZ materials, quoted with permission from Kinsey *et al.*[34]; (C) In a PC slab with a square lattice, an electrical monopole mode (the upper right panel) and a transverse magnetic (the lower left panel) form EMNZ, quoted with permission from Li *et al.*[36]; (D) Geometry of a 2D waveguide structure with an ENZ section to support the tunneling effect, quoted with permission from Silveirinha *et al.*[57]; (E) Sectional view of the ZIM cloaking shell covered by a metasurface, quoted with permission from Chu *et al.*[58]; (F) Photonic doping in the ENZ material, quoted with permission from Liberal *et al.*[59]; (G) Dispersion coding in the ENZ material based on photonic doping, quoted with permission from Zhou *et al.*[60]; (H) The enhanced absorption cross section when a resonator is doping, quoted with permission from Zhou *et al.*[76]; (I) ZIM can solve phase mismatching in the process of nonlinear propagation, quoted with permission from Suchowski *et al.*[77]; (J) Both BIC and ZIM realized in the daisy PC, quoted with permission from Minkov *et al.*[85]; (K) BIC (also called embedded eigenstate here) in a ENZ-dielectric-ENZ three-layered waveguide, quoted with permission from Monticone *et al.*[86]; (L) Concept of the secure targeted wireless power transfer, quoted with permission from Zanganeh *et al.*[87]; M: Magnetized gradient ENZ layer (the lower left panel) to realize broadband nonreciprocity breaking the classical Kirchhoff's law (the upper panel), quoted with permission from Liu *et al.*[90]. EMNZ: Epsilon-and-mu-near-zero; PC: photonic crystal;

ENZ: epsilon-near-zero; 2D: two-dimensional; ZIM: zero-index material; BIC: bound state in the continuum.

The tunneling effect[52-55,58-61,70-81]

Owing to the infinite effective spatial wavelength $\lambda \propto 1/n$ and the zero propagation phase nw/c, the characteristic length of structural deformation can be neglected. As a result, the electromagnetic wave can pass through a ZIM waveguide regardless of its shape, and the passing wavefront depends only on the shape of the waveguide's output port. This feature is leveraged to realize supercoupler[53-55], overcoming the limitation of evanescent fields in free space, and to achieve directional radiation[52,72-75], such as generating Bessel beams with the properties of non-diffraction and self-healing. Compared with the EMNZ, however, the impedance of ENZ/MNZ is infinite/zero, which generally leads to a mismatch with the input and output ports made of conventional materials. As a result, most energy is reflected instead of entering the waveguide. A feasible solution is to reduce the cross-sectional area of the waveguide, making at least one of the physical dimensions electrically small, as shown in Figure 4D[57,76-78]. On the other hand, the tunneling effect has also been observed in heterostructures composed of EMNZ media and complementary bianisotropic materials[79].

Similar differences also exist between EMNZ and ENZ/MNZ materials when considering doping impurities. For the environment outside the EMNZ material, impurities do not impact the passing electromagnetic wave, as if they are invisible, leading to potential applications such as cloaking, as shown in Figure 4E[52,58]. On the other hand, Liberal *et al.* propose that impurities in the ENZ material can modify the effective permeability of the entire medium. Intriguingly, owing to large phase velocities and static-like field distributions, this impact is independent of either the position of the impurities or the external geometry of ENZ materials, as shown in Figure 4F[59], which benefits robust information technology like dispersion coding in Figure 4G[60] and performing calculus[61].

To compensate for the divergent impedance mismatching between the ENZ material and the surrounding environment, Luo *et al.* designed a pair of parity-time-symmetry metasurfaces to sandwich the ENZ slab, effectively eliminating the scattering caused by impurities[80]. For impurities inside the ZIM, the absorption cross section can be significantly enhanced when a resonator is doping, as shown in Figure 4H[76], and the scattering cross section can be significantly enhanced when a scatter is doping[81].

The parameter enhancement[56,57,82]

In the nonlinear process, a major problem is the phase mismatch between nonlinear fields, which results in destructive interference and low generation efficiency. More specifically, material dispersion leads to a lack of photon momentum conservation. In ZIM, the photon momentum $p = h/\lambda$ is zero, preventing the conservation for any combination of directions, as shown in Figure 4I[77]. Moreover, based on the boundary condition of Maxwell's equations, $D_{\parallel} = \varepsilon E_{\parallel}$ and $B_{\parallel} = \mu H_{\parallel}$ are continuous across the interface, and the electric field 12 and/or the magnetic induction 12 are drastically enhanced in ZIM compared to the incident field. For Kerr-like nonlinearities, the intensity-dependent refractive index can be described by $n = \sqrt{\varepsilon^{(1)} + 3\chi^{(3)} | \boldsymbol{E} |^2}$, where $\chi^{(3)}$ is the third-order susceptibility. Hence, ZIM can enhance the nonlinear processes by enabling larger hysteresis and lower thresholds, which is beneficial for efficient and ultrathin all-optical switches or memories[56,82].

Likewise, the property of field enhancement is also utilized to improve the nonreciprocity arising from the magneto-optical effect. For example, by inducing a magnetized ENZ defect into a 1D PC, the defect modes in the band gap are shifted for forward and backward incidences. A similar phenomenon is also observed in heterostructures composed of a magnetized ENZ material and a truncated PC, and the Fano-type

interference with sharp spectral variation further enhances the shift.

The BIC[83-90]

As predicted by von Neumann and Wigner, the BIC is characterized by zero leakage and zero linewidth[83]. For ZIM slabs, the mechanism of BIC is employed to reduce the out-of-plane radiation loss. One approach is based on the symmetry-protected modes. A square lattice with C_{4v} symmetry supports a single 2D irreducible representation E, which corresponds to modes that couple to external plane waves. In comparison, the C_{6v} group has two distinct 2D irreducible representations E_1 and E_2 where modes belonging to E_2 do not couple to external plane waves. In that case, the triply degenerate point of EMNZ PC can be composed of modes from E_2, along with the 1D irreducible representations B_1 and B_2, as in the daisy PC shown in Figure 4J[84,85]. Another approach is based on the resonance-trapped modes. Considering the top and bottom interfaces of the slab as two mirrors, the thickness of this Fabry-Perot cavity can be tuned to induce destructive interference in each radiation channel[72,84].

Except for the PC slab, a kind of three-layered waveguide "ENZ-dielectric-ENZ" has been widely discussed to generate BIC (also called embedded eigenstates, EEs) in the past decade. At the frequency of the Fabry-Perot resonance in the dielectric layer, the ENZ layer with high impedance limits the leakage mode, as shown in Figure 4K[86], which promotes the targeted wireless power transfer (WPT) more securely, as shown in Figure 4L[87]. When a non-Hermitian parameter, like the loss in the ENZ layers, is considered, a pair of scattering singularities emerges from the BIC, and each singularity is protected by the topological charge $v = \int_C d\varphi_R = \pm 1$, where the anticlockwise closed loop C is around the singularity in the space composed of the frequency ω and the incident angle θ. The dramatic phase change is sensitive to the disturbance in the environment[88]. Moreover, when inducing the magneto-optical effect into ENZ layers, the nonreciprocal thermal radiation can break the classical Kirchhoff's law, i.e., the emissivity e (ω, θ) (forward) and the absorptivity α (ω, θ) (backward) are not equal[89]. Furthermore, taking gradient ENZ layers can realize broadband nonreciprocity, as shown in Figure 4M[90].

Beyond these theoretical mechanisms, ENZ-based architectures have also been widely leveraged in practical photonic devices. Several representative advances by Caputo and collaborators have demonstrated the versatility of ENZ metamaterials in nanoscale fabrication and functional photonic applications. One of the earlier works introduced multilayer ENZ nanocavities to enhance two-photon direct laser writing, achieving sub-50 nm resolution and enabling the fabrication of ultrathin metalenses and complex 3D nanostructures[91]. Building on similar photonic structures, the group later developed anticounterfeiting tags by embedding QR codes beneath plasmonic multilayers on paper substrates. These tags exhibited unique speckle patterns and structural colors, functioning as physical unclonable functions (PUFs) for secure optical authentication[92]. Subsequently, ENZ nanocavities were combined with metasurfaces to engineer Fano-Rabi resonances with ultra-narrow spectral features and high refractive index sensitivity, offering promising capabilities for label-free biochemical sensing[93]. In a further step, the researchers introduced tunable optical coupling by inserting a birefringent liquid crystal layer between ENZ cavities, enabling polarization-sensitive spectral splitting and reconfigurable resonance modes[94]. These works collectively demonstrate a transition from passive ENZ-based nanostructures to tunable, multifunctional photonic systems, reinforcing the relevance of ENZ metamaterials in the broader context of meta-crystal research.

PMC WITH HMM

In most situations of the above-mentioned discussions, the material anisotropy shown in Figure 5A[28,95], whether natural or artificial, is neglected. For metamaterials, substituting periodicity with continuous translation symmetry in one or two spatial dimensions, such as in metal-dielectric multilayer film or

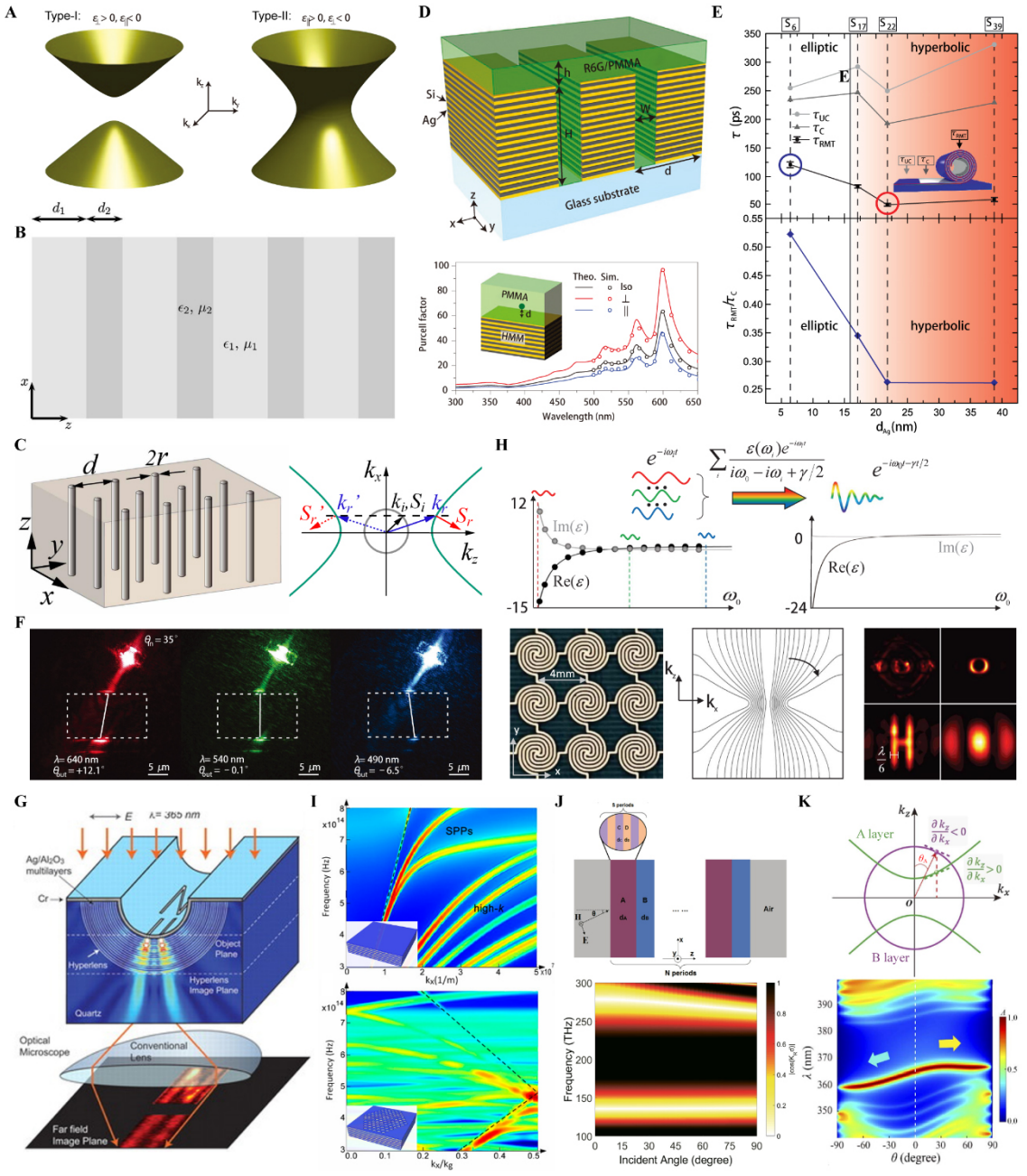

Figure 5. (A) The IFC in the HMM, quoted with permission from Poddubny *et al.*[28]; (B) The metal-dielectric multilayer film, quoted with permission from Wood *et al.*[30]; (C) The nanowire array (the left panel) and the negative refraction analyzed through the IFC (the right panel), quoted with permission from Liu *et al.*[32]; (D) The enhanced spontaneous emission in multilayer HMM, quoted with permission from Lu *et al.*[35]; (E) The enhancement during the topological transition between elliptic and hyperbolic dispersions, quoted with permission from Schulz *et al.*[62]; (F) The transition between positive and negative refractions in HMM, quoted with permission from High *et al.*[102]; (G) The magnifying super lens, quoted with permission from Liu *et al.*[104]; (H) The strategy of complex frequency composed of multiple real frequencies (the upper panel) and related imaging of the super lens (the lower panel), quoted with permission from Guan *et al.*[105]; (I) The band structures and schematics of the HMM (the upper panel) and the 2D hypercrystal (the lower panel), quoted with permission from Galfsky *et al.*[106]; (J) The schematic of the 1D hypercrystal (the upper panel) and the dispersionless band gap (the lower panel), quoted with permission from Xue *et al.*[108]; (K) The phase variation compensation in the IFC (the upper panel) and the forward dispersionless and backward monotonic increasing band gap in magnetized 1D hypercrystal (the lower panel), quoted with permission from Hu *et al.*[109]. IFC: Isofrequency contour; HMM: hyperbolic metamaterial; 2D: two-dimensional.

nanowire array, may lead to extreme anisotropy. According to EMT, the permittivity can be described as $\varepsilon_\perp = f\varepsilon_1 + (1-f)\varepsilon_2$, $\varepsilon_\parallel = 1/[f/\varepsilon_1 + (1-f)/\varepsilon_2]$ for the metal-dielectric multilayer film, as shown in Figure 5B[29], and as $\varepsilon_\perp = \varepsilon_2 + \frac{f\varepsilon_2(\varepsilon_1-\varepsilon_2)}{\varepsilon_2 + (1-f)(\varepsilon_1-\varepsilon_2)q_{eff}}$, $\varepsilon_\parallel = f\varepsilon_1 + (1-f)\varepsilon_2$ for the nanowire array in Figure 5C[32]. Here, the subscripts 1 and 2 denote the metal and dielectric, respectively. The filling ratio of metal is defined as $f = d_1/(d_1 + d_2)$ for the multilayer film, where d_1 and d_2 are the thickness of the metal and dielectric layers. For the nanowire array, the filling ratio is defined as $f = 2\pi r^2/(\sqrt{3}d^2)$, where r is the nanowire radius and d is the spacing between adjacent nanowires. The parameter q_{eff} represents the effective depolarization factor. For the TM polarization, the dispersion of the isofrequency contour (IFC) follows the dispersion relation $k_\perp^2/\varepsilon_\parallel + k_\parallel^2/\varepsilon_\perp = (\omega/c)^2$. This expression results in a closed elliptical contour in conventional dielectrics. However, when $\varepsilon_\parallel \cdot \varepsilon_\perp < 0$, the contour becomes open hyperbolic, and the name "Hyperbolic metamaterial" is derived. More specifically, $\varepsilon_\perp < 0$, $\varepsilon_\parallel > 0$ corresponds to type I or the dielectric-type, and $\varepsilon_\perp > 0$, $\varepsilon_\parallel < 0$ corresponds to type II or the metal-type, as shown in Figure 5A. In addition to artificial structures, recent studies have found that natural van der Waals materials may become potential candidates with hyperbolic dispersions[95], such as α-MoO_3 with phonon polaritons (PhPs)[96,97] and β-Ga_2O_3 with shear polaritons (ShPs)[98,99]. Notably, most unique properties of HMMs, both natural and artificial, originate from the hyperbolic topology of IFC.

The enhanced spontaneous emission[27,38,62,100,101]

The photonic density of states (DOS) is related to the volume between the dispersion of $\omega(\boldsymbol{k})$ and $\omega(\boldsymbol{k}) + d\omega$[100]. Therefore, the HMM with an open IFC theoretically exhibits infinite DOS, where high wavevectors also contribute. Although the DOS of HMMs in practice is limited by several factors, including the ohmic losses of the metal components, the dispersion of the dielectric components, the finite period of the metamaterial, the finite size of source, and the finite distance between the source and the metamaterial[27], the spontaneous emission can still be enhanced by using a grating-like HMM with the outcoupling effect, as shown in Figure 5D[35]. Furthermore, spontaneous emission can be flexibly modulated by altering the filling ratio, which leads to improvement during the topological transition between elliptic and hyperbolic dispersions, as shown in Figure 5E[62]. Additionally, HMMs exhibit anomalous scaling laws: cavities with different sizes can share the same resonant frequency, and higher-order resonance modes can oscillate at lower frequencies. This property offers a strategy for reducing the size of HMM structures to increase the quality factor and enhance the light-matter interactions[101].

The negative refraction[32,102,103]

Considering an incident light with momentum k_i and the Poynting vector S_i from the isotropic dielectric, the conservation of the tangential momentum determines two possible refraction momentum k_r and k_r' after passing through the interface between the dielectric and the HMM. Then, the causality principle determines S_r flowing away from the interface, which corresponds to a negative refraction angle $\theta_{r,S} = \tan^{-1}(\frac{k_x/\varepsilon_z}{k_z/\varepsilon_x})$, as shown in Figures 5C and F[32,102]. It is worth mentioning that the anisotropic permittivity only affects the TM polarization, while the TE polarization maintains the positive refraction[103].

The super lens[103-109]

In far-field imaging, the high-frequency information is evanescent and lost in the dielectric. In comparison, the HMM with an open IFC can support this kind of information, and transfer the near-field information to the other side, thereby breaking the diffraction limit of light. A cylindrical HMM is designed to magnify the image, as shown in Figure 5G[104]. While the functionality of the super lens is well described by EMT, it is important to note that EMT assumes deeply subwavelength structuring and a local electromagnetic response. However, in practice, these assumptions may become less accurate when the structural periodicity approaches the operating wavelength or when high-k modes dominate the imaging process. Under such conditions, the actual dispersion and energy transport behavior may deviate from EMT-based predictions,

especially near the topological transition region. To improve modeling accuracy, full-wave simulations are typically used in parallel with EMT during the design stage. Moreover, naturally hyperbolic materials such as α-MoO_3 and h-BN offer a promising alternative, achieving broadband hyperbolic dispersion without relying on structural averaging. To compensate for intrinsic losses, a recent study proposed an excitation with a complex frequency composed of multiple real frequencies, as shown in Figure 5H[105].

While HMMs exhibit topology in the form of open IFCs, this geometrical topology differs from the band topology discussed in topological photonics. The former arises from anisotropic dispersion and leads to phenomena such as high-k modes and enhanced density of states, whereas the latter is characterized by global invariants such as the Berry phase or the Zak phase, which guarantee robust surface or edge states. Incorporating HMMs into PCs provides a natural bridge between IFC engineering and band topology, enabling new topological phases such as Type-I, II, and III nodal semimetals. This synergy underpins many recent advances in PCMs and sets the stage for the discussion of topological phenomena in the following section.

To some extent, the advantages of HMM and PC are complementary. By integrating HMM with PC, the concept of the photonic hypercrystal has been proposed[103]. On the one hand, HMMs possess a broadband DOS, but the high-momentum modes lie below the light line, trapping most of the emitted power inside the HMM. By patterning a 2D lattice of holes, the periodicity can fold these modes inside the light line like PCM, and provide high light-scattering efficiency with the surrounding environment, as shown in Figure 5I[106,107]. On the other hand, the band gap of PC, especially in conventional all-dielectric designs, tends to exhibit blue shift dispersion with increasing incident angle, since the group velocity (associated with the Poynting vector) is positive in the dielectric. In comparison, HMMs with negative group velocity can introduce a new degree of freedom to modulate the band gap. When the condition of phase variation compensation $d_B / d_A = -\sqrt{\varepsilon_{A\perp}\varepsilon_B} / \varepsilon_{A\parallel}$ is fulfilled, even a dispersionless band gap can be realized in the hypercrystal composed of HMM layer A and dielectric layer B. Here, the subscripts 1 and 2 denote the HMM and dielectric components in the hypercrystal, respectively, as shown in Figure 5J[108]. Furthermore, the induced magneto-optical effect can provide a flexible degree of monotonicity to the band gap, such as monotonic increasing in the whole k_x space, or forward dispersionless and backward monotonic increasing. It may facilitate applications such as unidirectional optical absorbers in a wide-angle range, as shown in Figure 5K[109].

PMC AND TOPOLOGY

Beyond Landau's classic approach based on spontaneously broken symmetries, topological theory provides a new perspective on the classification paradigm, including gapped phases such as topological insulators[110], and gapless phases such as topological semimetals[111]. After the realization of topological insulators[112-114], photonic systems, especially PCs and metamaterials, have also been proven to be versatile platforms to demonstrate the phases of topological semimetals, which can be further classified into nodal points[115,116], nodal lines[117,118], and nodal surfaces[119] according to the dimensions of band degeneracy areas. A growing frontier in this field is to emulate relativistic quasiparticles that feature band degeneracies with linear dispersions, such as fourfold Dirac fermions and even twofold Weyl fermions. However, most of the designs are based on 2D lattices, and it is highly desirable in practice to use a simpler 1D lattice to realize similar band structures.

In 1D PCs with inversion symmetry, the imaginary part of the surface impedance ς is dictated by the cumulative Zak phases of the bulk bands below the nth gap: $sgn[\varsigma^{(n)}] = (-1)^n(-1)^l exp(i\sum_{m=0}^{n-1}\theta_m^{Zak})$, where l counts the number of band crossings, and θ_m^{Zak} represents the Zak phase of the mth bulk band. This "bulk-interface

correspondence" ensures the presence of interface states when $\varsigma_L + \varsigma_R = 0$, analogous to the SSH model but implemented through classical impedance. Tuning parameters (e.g., permittivity) across a topological transition reverses the sign of ς via Zak phase inversion, enabling robust interface states even in graded-index systems[68]. In 2021, the condition of band degeneracy $\tilde{n}_A d_A / \tilde{n}_B d_B \in \mathbb{Q}$ was proposed for a 1D PC composed of alternating layers of dielectrics A and B, where $\tilde{n}_i = \sqrt{\varepsilon_i \mu_i - k_x^2 / k_0^2}\,(i = A, B)$. Owing to the in-plane isotropy in the x - y space, the azimuth angle φ does not affect the transmission spectrum. As a result, linear degeneracy extends to form a nodal ring in the k_x - k_y space, which can be perceived as a photonic Dirac nodal line semimetal. By truncating the PC with a silver film (playing the role of ENG materials), a surface state can exist in the MNG band gap for both TE and TM polarizations. This results in a double-bowl state, as shown in Figure 6A[37]. Furthermore, the surface state is shown to be protected by the π-Berry phase (In 1D systems, the Berry phase corresponds to the previously mentioned Zak phase), where a 2π reflection phase winds around the ring. When inversion symmetry is broken, the nodal ring will be gapped, and the π-Berry phase will diffuse into a toroidal-shaped Berry flux. This gives rise to photonic ridge states, as shown in Figure 6B[120,121]. The above-mentioned two designs are based on all-dielectric PCs, where the group velocity remains positive throughout the structure, corresponding to Type-II phases. By introducing HMM, the group velocity of the hypercrystal can be modulated by altering the thickness ratio between HMM layer A and dielectric layer B, enabling a phase transition from Type-II to critical Type-III and eventually to Type-I. In addition, the Fermi energy of the graphene can be tuned to realize the DOF of translation between Dirac, quasi-Dirac, and isolated Weyl phases, as shown in Figure 6C. For the unit cells without the inversion symmetry, both sides of the band gap contain ENG and MNG components. Therefore, a pair of reflection-phase topological charges emerge near each degenerate point. These charges pin a novel bilateral drumhead surface state for both TE and TM waves, spanning both the inner and outer regions of the degenerate point in the projected surface Brillouin zone. Intriguingly, the charges within the gap are analogous to events with causal relationships restricted to the time-like region of the light cone. As the number of unit cells increases, the pair of charges gradually approaches each other but cannot cross the band edge or fully annihilate. This behavior leads to the formation of a quasi-BIC. Such a phenomenon appears simultaneously in Dirac, quasi-Dirac, and isolated Weyl phases, and may serve as a potential bridge between singularity physics and nodal physics, as shown in Figure 6D[122].

While significant progress has been made in designing topological phases within photonic meta-crystals, several practical challenges that limit their implementation in real-world systems remain. These include the limited tunability of band structures in static lattices, the difficulty of achieving nonreciprocal transport without bulky configurations or strong bias fields, and the integration challenges posed by resonant or large-footprint components. These limitations can hinder the realization of compact, reconfigurable, and broadband topological functionalities in integrated photonic platforms. Recent studies have started to address these issues. For example, reconfigurable van der Waals heterostructures, such as trilayer α-MoO_3, enable real-time control over topological dispersion through multiple robust photonic magic angles, providing a flexible alternative to traditional rigid photonic crystals[97]. In addition, shear polaritons observed in β-Ga_2O_3 provide an intrinsic mechanism for directional wave propagation, without requiring structural asymmetry or complex patterning[99]. Furthermore, broadband nonreciprocal absorption has been demonstrated in magnetized gradient ENZ films, enabling directional light control in ultrathin, non-resonant structures that are suitable for on-chip integration[89]. These advances not only help overcome current limitations in PMC-based designs but also highlight their increasing potential in integrated, reconfigurable, and topologically robust optical systems.

CONCLUSIONS

PC and metamaterial, both periodic structures composed of unit cells with different characteristic scales,

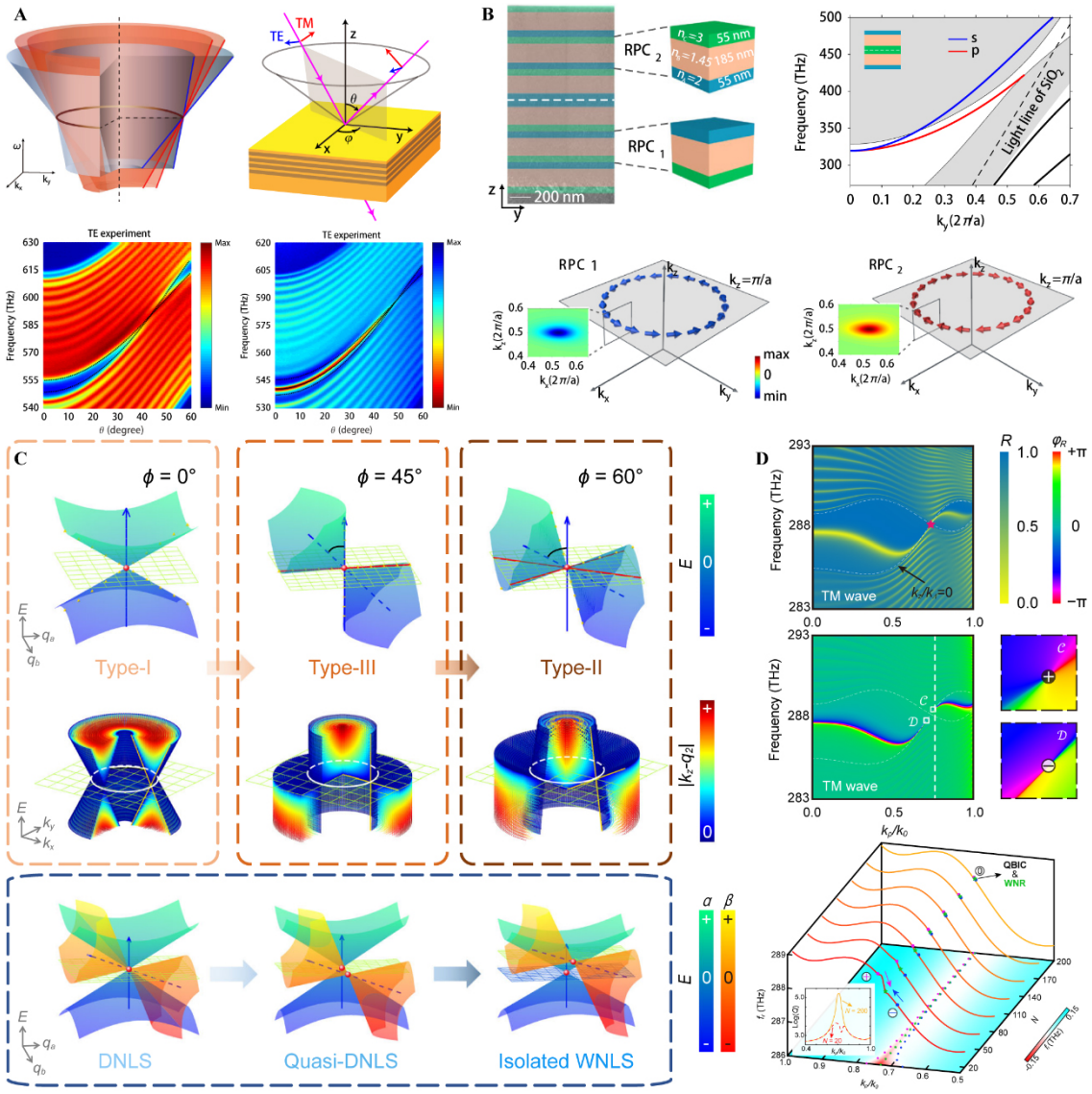

Figure 6. (A) The sketch of the in-plane dispersion around the Dirac nodal ring (the upper left panel), the experimental setup (the upper right panel), the transmission spectra of the PC to observe the Dirac nodal ring (the lower left panel, the situation of the TM mode is similar), and the double-bowl state for the truncated PC (the lower right panel, the situation of the TM mode is similar), quoted with permission from Hu *et al.*[37]; (B) The schematic of PC without the inversion symmetry (the upper left panel), the gapped ridge state (the upper right panel), and the toroidal-shaped Berry fluxes for vortexes for two structures (the lower panel), quoted with permission from Deng *et al.*[120]; (C) The degree of freedom of rotation and translation in the hypercrystal; (D) The bilateral drumhead surface state (the upper panel) is pinned by a pair of reflection-phase topological charges (the middle panel), and the charge pair approaches each other, but cannot annihilate completely, which forms a quasi-BIC (the lower panel), quoted with permission from Hu *et al.*[122]. PC: Photonic crystal; TM: transverse magnetic; BIC: bound state in the continuum.

have promoted the explorations of novel phenomena over the past two decades, some of which even violate and reshape conventional cognitions. To some extent, the advantages of PC and metamaterial are complementary, and their combination is becoming a paradigm in the photonics community. Photonic meta-crystals, by integrating these features, have emerged as a powerful hybrid paradigm that enables unprecedented tunability of photonic band structures. This review has provided a comprehensive classification of PMCs based on their electromagnetic responses, including LHMs, SNG materials, ZIMs, and HMMs. Compared to earlier reviews that examined PCs or metamaterials in isolation, this article

bridges both theoretical foundations and experimental realizations of PMCs, presenting a unified framework that links electromagnetic parameters to emerging functionalities. In particular, PMCs offer distinctive advantages in enabling topological phenomena - such as photonic Dirac/Weyl semimetals, double-bowl states, and quasi-BICs - through precise engineering of symmetry, band degeneracies, and reflection-phase topology. Furthermore, the extreme field enhancement in ZIM-based structures greatly facilitates nonlinear optical amplification, reducing device size and energy thresholds. The introduction of magneto-optical effects and gain/loss modulation also provides new pathways for achieving broadband nonreciprocal light transport, which is crucial for isolators and unidirectional emitters. However, fabrication processes that bridge two scales with significant differences may be more complicated. Recent advances in van der Waals materials indicate their potential as candidates for metamaterials, possibly offering a feasible way for the next generation of robust and miniaturized devices. Looking forward, PMCs hold great potential for transformative impact in integrated photonics and quantum optics. In integrated systems, they can act as topologically protected waveguides, low-threshold nonlinear switches, or nonreciprocal elements in photonic circuits. In quantum regimes, the engineered density of photonic states and tunable emission dynamics of PMCs may enable efficient single-photon sources, quantum interfaces, and entanglement-preserving photonic channels. The vast design space offered by anisotropy, periodicity, magnetism, and gain/loss further facilitates exploration in emerging fields such as optical neural networks, programmable metasurfaces, and quantum sensing. Overall, this review highlights the unique physical mechanisms, multifunctional capabilities, and practical prospects of PMCs, positioning them as a frontier architecture for topological photonics, nonlinear optics, and next-generation integrated and quantum photonic systems.

DECLARATIONS

Authors' contributions

Conceptualization and supervision: Chen, H.; Guo, Z.
Writing-original draft, writing-review and editing: Hu, S.; Li, P.; Chen, H.; Guo, Z.
Funding acquisition: Guo, Z.

Availability of data and materials

Not applicable.

Financial support and sponsorship

This work was supported by the National Key R&D Program of China (Nos. 2021YFA1400602 and 2023YFA1407600), the National Natural Science Foundation of China (Nos. 12004284 and 12374294), and the Chenguang Program of Shanghai Education Development Foundation and Shanghai Municipal Education Commission (No. 21CGA22).

Conflicts of interest

All authors declared that there are no conflicts of interest.

Ethical approval and consent to participate

Not applicable.

Consent for publication

Not applicable.

REFERENCES

1. Bloch, F. Über die quantenmechanik der elektronen in kristallgittern. *Z. Physik.* **1929**, *52*, 555-600. (in German). DOI
2. Yablonovitch, E. Inhibited spontaneous emission in solid-state physics and electronics. *Phys. Rev. Lett.* **1987**, *58*, 2059-62. DOI PubMed
3. John, S. Strong localization of photons in certain disordered dielectric superlattices. *Phys. Rev. Lett.* **1987**, *58*, 2486-9. DOI PubMed
4. Dudley, J. M.; Genty, G.; Coen, S. Supercontinuum generation in photonic crystal fiber. *Rev. Mod. Phys.* **2006**, *78*, 1135-84. DOI
5. Vaidya, S.; Benalcazar, W. A.; Cerjan, A.; Rechtsman, M. C. Point-defect-localized bound states in the continuum in photonic crystals and structured fibers. *Phys. Rev. Lett.* **2021**, *127*, 023605. DOI PubMed
6. Tyumenev, R.; Hammer, J.; Joly, N. Y.; Russell, P. S. J.; Novoa, D. Tunable and state-preserving frequency conversion of single photons in hydrogen. *Science* **2022**, *376*, 621-4. DOI PubMed
7. Bonsma-Fisher, K. A. G.; Bustard, P. J.; Parry, C.; et al. Ultratunable quantum frequency conversion in photonic crystal fiber. *Phys. Rev. Lett.* **2022**, *129*, 203603. DOI
8. Martínez L, Wiedemann P, Zhu C, Geilen A, Stiller B. Optoacoustic cooling of traveling hypersound waves. *Phys. Rev. Lett.* **2024**, *132*, 023603. DOI PubMed
9. Morita, R.; Inoue, T.; De, Z. M.; Ishizaki, K.; Noda, S. Photonic-crystal lasers with two-dimensionally arranged gain and loss sections for high-peak-power short-pulse operation. *Nat. Photonics.* **2021**, *15*, 311-8. DOI
10. Yoshida, M.; Katsuno, S.; Inoue, T.; et al. High-brightness scalable continuous-wave single-mode photonic-crystal laser. *Nature* **2023**, *618*, 727-32. DOI PubMed PMC
11. Fushman, I.; Englund, D.; Faraon, A.; Stoltz, N.; Petroff, P.; Vuckovic, J. Controlled phase shifts with a single quantum dot. *Science* **2008**, *320*, 769-72. DOI PubMed
12. Gu, T.; Petrone, N.; Mcmillan, J. F.; et al. Regenerative oscillation and four-wave mixing in graphene optoelectronics. *Nature. Photon.* **2012**, *6*, 554-9. DOI
13. Zangeneh-Nejad, F.; Fleury, R. Topological analog signal processing. *Nat. Commun.* **2019**, *10*, 2058. DOI PubMed PMC
14. Wang, H.; Guo, C.; Zhao, Z.; Fan, S. Compact incoherent image differentiation with nanophotonic structures. *ACS. Photonics.* **2020**, *7*, 338-43. DOI
15. Guo, C.; Xiao, M.; Minkov, M.; Shi, Y.; Fan, S. Photonic crystal slab Laplace operator for image differentiation. *Optica* **2018**, *5*, 251. DOI
16. Zhou, Y.; Zheng, H.; Kravchenko, I. I.; Valentine, J. Flat optics for image differentiation. *Nat. Photonics.* **2020**, *14*, 316-23. DOI
17. Zhu, D.; Zhang, Y. H.; Liu, S. J.; et al. Polychromatic dual-mode imaging with structured chiral photonic crystals. *Nano. Lett.* **2024**, *24*, 140-7. DOI
18. Zhao, Q.; Zhou, J.; Zhang, F.; Lippens, D. Mie resonance-based dielectric metamaterials. *Mater. Today.* **2009**, *12*, 60-9. DOI
19. Ginn, J. C.; Brener, I.; Peters, D. W.; et al. Realizing optical magnetism from dielectric metamaterials. *Phys. Rev. Lett.* **2012**, *108*, 097402. DOI
20. Rybin, M. V.; Filonov, D. S.; Samusev, K. B.; Belov, P. A.; Kivshar, Y. S.; Limonov, M. F. Phase diagram for the transition from photonic crystals to dielectric metamaterials. *Nat. Commun.* **2015**, *6*, 10102. DOI PubMed PMC
21. Tuz, V. R. Polaritons dispersion in a composite ferrite-semiconductor structure near gyrotropic-nihility state. *J. Magn. Magn. Mater.* **2016**, *419*, 559-65. DOI
22. Kadic, M.; Milton, G. W.; van Hecke, M.; Wegener, M. 3D metamaterials. *Nat. Rev. Phys.* **2019**, *1*, 198-210. DOI
23. Pendry, J. B.; Schurig, D.; Smith, D. R. Controlling electromagnetic fields. *Science* **2006**, *312*, 1780-2. DOI PubMed
24. Schurig, D.; Mock, J. J.; Justice, B. J.; et al. Metamaterial electromagnetic cloak at microwave frequencies. *Science* **2006**, *314*, 977-80. DOI
25. Liu, R.; Ji, C.; Mock, J. J.; Chin, J. Y.; Cui, T. J.; Smith, D. R. Broadband ground-plane cloak. *Science* **2009**, *323*, 366-9. DOI PubMed
26. Shelby, R. A.; Smith, D. R.; Schultz, S. Experimental verification of a negative index of refraction. *Science* **2001**, *292*, 77-79. DOI
27. Valentine, J.; Zhang, S.; Zentgraf, T.; et al. Three-dimensional optical metamaterial with a negative refractive index. *Nature* **2008**, *455*, 376-9. DOI PubMed
28. Poddubny, A.; Iorsh, I.; Belov, P.; Kivshar, Y. Hyperbolic metamaterials. *Nat. Photonics.* **2013**, *7*, 948-57. DOI
29. Liu, Z. W.; Lee, H.; Xiong, Y.; Sun, C.; Zhang, X. Far-field optical hyperlens magnifying sub-diffraction-limited objects. *Science* **2007**, *315*, 1686. DOI
30. Wood, B.; Pendry, J. B.; Tsai, D. P. Directed subwavelength imaging using a layered metal-dielectric system. *Phys. Rev. B.* **2006**, *74*, 115116-48. DOI
31. Kim, S.; Peng, Y. G.; Yves, S.; Alù, A. Loss compensation and superresolution in metamaterials with excitations at complex frequencies. *Phys. Rev.* **2023**, *13*, 041024. DOI
32. Liu, Y.; Bartal, G.; Zhang, X. All-angle negative refraction and imaging in a bulk medium made of metallic nanowires in the visible region. *Opt. Express.* **2008**, *16*, 15439-48. DOI

33. Dai, J.; Jiang, H.; Guo, Z.; Qiu, J. Tunable epsilon-and-mu-near-zero metacomposites. *Adv. Funct. Mater.* **2024**, *34*, 2308338. DOI
34. Kinsey, N.; Devault, C.; Boltasseva, A.; Shalaev, V. M. Near-zero-index materials for photonics. *Nat. Rev. Mater.* **2023**, *8*, 742-60. DOI
35. Lu, D.; Kan, J. J.; Fullerton, E. E.; Liu, Z. W. Enhancing spontaneous emission rates of molecules using nanopatterned multilayer hyperbolic metamaterials. *Nat. Nanotechnol.* **2014**, *9*, 48-53. DOI PubMed
36. Li, Y.; Chan, C. T.; Mazur, E. Dirac-like cone-based electromagnetic zero-index metamaterials. *Light. Sci. Appl.* **2021**, *10*, 203. DOI PubMed PMC
37. Hu, M.; Zhang, Y.; Jiang, X.; et al. Double-bowl state in photonic Dirac nodal line semimetal. *Light. Sci. Appl.* **2021**, *10*, 170. DOI PubMed PMC
38. Li, J.; Zhou, L.; Chan, C. T.; Sheng, P. Photonic band gap from a stack of positive and negative index materials. *Phys. Rev. Lett.* **2003**, *90*, 083901. DOI
39. Pendry, J. B. Negative refraction makes a perfect lens. *Phys. Rev. Lett.* **2000**, *85*, 3966-9. DOI PubMed
40. Liu, W.; Chen, J.; Li, T.; et al. Imaging with an ultrathin reciprocal lens. *Phys. Rev. X.* **2023**, *13*, 031039. DOI
41. Seddon, N.; Bearpark, T. Observation of the inverse Doppler effect. *Science* **2003**, *302*, 1537-40. DOI PubMed
42. Kozyrev, A. B.; van der Weide, D. W. Explanation of the inverse Doppler effect observed in nonlinear transmission lines. *Phys. Rev. Lett.* **2005**, *94*, 203902. DOI PubMed
43. Chen, J.; Wang, Y.; Jia, B.; et al. Observation of the inverse Doppler effect in negative-index materials at optical frequencies. *Nature. Photon.* **2011**, *5*, 239-42. DOI
44. Xi, S.; Chen, H.; Jiang, T.; et al. Experimental verification of reversed Cherenkov radiation in left-handed metamaterial. *Phys. Rev. Lett.* **2009**, *103*, 194801. DOI
45. Hummelt, J. S.; Lu, X.; Xu, H.; Mastovsky, I.; Shapiro, M. A.; Temkin, R. J. Coherent Cherenkov-cyclotron radiation excited by an electron beam in a metamaterial waveguide. *Phys. Rev. Lett.* **2016**, *117*, 237701. DOI
46. Duan, Z.; Tang, X.; Wang, Z.; et al. Observation of the reversed Cherenkov radiation. *Nat. Commun.* **2017**, *8*, 14901. DOI PubMed PMC
47. Guo, X.; Wu, C.; Zhang, S.; et al. Mid-infrared analogue polaritonic reversed Cherenkov radiation in natural anisotropic crystals. *Nat. Commun.* **2023**, *14*, 2532. DOI PubMed PMC
48. Alu, A.; Engheta, N. Pairing an epsilon-negative slab with a mu-negative slab: Resonance, tunneling and transparency. *IEEE. Trans. Antennas. Propagat.* **2003**, *51*, 2558-71. DOI
49. Ginis, V.; Tassin, P.; Soukoulis, C. M.; Veretennicoff, I. Enhancing optical gradient forces with metamaterials. *Phys. Rev. Lett.* **2013**, *110*, 057401. DOI PubMed
50. Kaina, N.; Lemoult, F.; Fink, M.; Lerosey, G. Negative refractive index and acoustic superlens from multiple scattering in single negative metamaterials. *Nature* **2015**, *525*, 77-81. DOI PubMed
51. Long, Y.; Ren, J.; Guo, Z.; et al. Designing all-electric subwavelength metasources for near-field photonic routings. *Phys. Rev. Lett.* **2020**, *125*, 157401. DOI
52. Huang, X.; Lai, Y.; Hang, Z. H.; Zheng, H.; Chan, C. T. Dirac cones induced by accidental degeneracy in photonic crystals and zero-refractive-index materials. *Nat. Mater.* **2011**, *10*, 582-6. DOI
53. Ma H, Hui Shi J, Cheng Q, Jun Cui T. Experimental verification of supercoupling and cloaking using mu-near-zero materials based on a waveguide. *Appl. Phys. Lett.* **2013**, *103*, 021908. DOI
54. Yang, Y.; Liu, Y.; Qin, J.; et al. Magnetically tunable zero-index metamaterials. *Photon. Res.* **2023**, *11*, 1613. DOI
55. Yan, W.; Zhou, Z.; Li, H.; Li, Y. Transmission-type photonic doping for high-efficiency epsilon-near-zero supercoupling. *Nat. Commun.* **2023**, *14*, 6154. DOI PubMed PMC
56. Reshef, O.; De, L. I.; Alam, M. Z.; Boyd, R. W. Nonlinear optical effects in epsilon-near-zero media. *Nat. Rev. Mater.* **2019**, *4*, 535-51. DOI
57. Silveirinha, M.; Engheta, N. Tunneling of electromagnetic energy through subwavelength channels and bends using ε-near-zero materials. *eLight* **2024**, *4*, 59. DOI
58. Chu, H.; Li, Q.; Liu, B.; et al. A hybrid invisibility cloak based on integration of transparent metasurfaces and zero-index materials. *Light. Sci. Appl.* **2018**, *7*, 50. DOI PubMed PMC
59. Liberal, I.; Mahmoud, A. M.; Li, Y.; Edwards, B.; Engheta, N. Photonic doping of epsilon-near-zero media. *Science* **2017**, *355*, 1058-62. DOI PubMed
60. Zhou, Z. H.; Li, H.; Sun, W. Y.; et al. Dispersion coding of ENZ media via multiple photonic dopants. *Light-Sci. Appl.* **2022**, *11*, 207. DOI
61. Li, H.; Fu, P.; Zhou, Z.; et al. Performing calculus with epsilon-near-zero metamaterials. *Sci. Adv.* **2022**, *8*, eabq6198. DOI PubMed PMC
62. Schulz, K. M.; Vu, H.; Schwaiger, S.; et al. Controlling the spontaneous emission rate of quantum wells in rolled-up hyperbolic metamaterials. *Phys. Rev. Lett.* **2016**, *117*, 085503. DOI
63. Veselago, V. G. The electrodynamics of substances with simultaneously negative values of ε and μ. *Sov. Phys. Usp.* **1968**, *10*, 509-14. DOI
64. Shadrivov, I. V.; Sukhorukov, A. A.; Kivshar, Y. S. Complete band gaps in one-dimensional left-handed periodic structures. *Phys. Rev. Lett.* **2005**, *95*, 193903. DOI PubMed

65. Căbuz, A. I.; Felbacq, D.; Cassagne, D. Homogenization of negative-index composite metamaterials: a two-step approach. *Phys. Rev. Lett.* **2007**, *98*, 037403. DOI PubMed
66. Zhu, X.; Liang, B.; Kan, W.; Zou, X.; Cheng, J. Acoustic cloaking by a superlens with single-negative materials. *Phys. Rev. Lett.* **2011**, *106*, 014301. DOI
67. Shi, X.; Xue, C.; Jiang, H.; Chen, H. Topological description for gaps of one-dimensional symmetric all-dielectric photonic crystals. *Opt. Express.* **2016**, *24*, 18580-91. DOI
68. Xiao, M.; Zhang, Z.; Chan, C. Surface impedance and bulk band geometric phases in one-dimensional systems. *Phys. Rev. X.* **2014**, *4*, 021017. DOI
69. Edwards, B.; Alù, A.; Young, M. E.; Silveirinha, M.; Engheta, N. Experimental verification of epsilon-near-zero metamaterial coupling and energy squeezing using a microwave waveguide. *Phys. Rev. Lett.* **2008**, *100*, 033903. DOI PubMed
70. Wang, N.; Zhang, R.; Chan, C. T.; Wang, G. P. Effective medium theory for a photonic pseudospin-1/2 system. *Phys. Rev. B.* **2020**, *102*, 094312. DOI
71. Dong, T.; Liang, J.; Camayd-Muñoz, S.; et al. Ultra-low-loss on-chip zero-index materials. *Light. Sci. Appl.* **2021**, *10*, 10. DOI PubMed PMC
72. Jiang, H.; Liu, W.; Yu, K.; et al. Experimental verification of loss-induced field enhancement and collimation in anisotropic μ-near-zero metamaterials. *Phys. Rev. B.* **2015**, *91*, 045302. DOI
73. Li, H.; Zhou, Z.; He, Y.; et al. Geometry-independent antenna based on epsilon-near-zero medium. *Nat. Commun.* **2022**, *13*, 3568. DOI PubMed PMC
74. Hwang, J. S.; Xu, J.; Raman, A. P. Simultaneous control of spectral and directional emissivity with gradient epsilon-near-zero inas photonic structures. *Adv. Mater.* **2023**, *35*, e2302956. DOI PubMed
75. Liu, Y. Y.; Dong, T.; Qin, X.; et al. High-permittivity ceramics enabled highly homogeneous zero-index metamaterials for high-directivity antennas and beyond. *eLight* **2024**, *4*, 59. DOI
76. Zhou, M.; Shi, L.; Yu, Z. F. Extraordinarily large optical cross section for localized single nanoresonator. *Phys. Rev. Lett.* **2015**, *115*, 023903. DOI
77. Suchowski, H.; O'Brien, K.; Wong, Z. J.; Salandrino, A.; Yin, X. B.; Zhang, X. Phase mismatch–free nonlinear propagation in optical zero-index materials. *Science* **2013**, *342*, 1223-6. DOI PubMed
78. Liu, R.; Cheng, Q.; Hand, T.; et al. Experimental demonstration of electromagnetic tunneling through an epsilon-near-zero metamaterial at microwave frequencies. *Phys. Rev. Lett.* **2008**, *100*, 023903. DOI
79. Chen, M. L. N.; Bi, Y.; Chan, H. C.; Lin, Z.; Ma, S.; Zhang, S. Anomalous electromagnetic tunneling in bianisotropic ϵ-μ-zero media. *Phys. Rev. Lett.* **2022**, *129*, 123901. DOI
80. Luo, J.; Li, J.; Lai, Y. Electromagnetic impurity-immunity induced by parity-time symmetry. *Phys. Rev. X.* **2018**, *8*, 031035. DOI
81. Wang, C.; Qian, C.; Hu, H.; et al. Superscattering of light in refractive-index near-zero environments. *PIER.* **2020**, *168*, 15-23. DOI
82. Argyropoulos, C.; Chen, P.; D'aguanno, G.; Engheta, N.; Alù, A. Boosting optical nonlinearities in ε-near-zero plasmonic channels. *Phys. Rev. B.* **2012**, *85*, 045129. DOI
83. von Neumann J, Wigner EP. Über merkwürdige diskrete eigenwerte. In: Wightman AS, editor. The Collected Works of Eugene Paul Wigner. Berlin: Springer Berlin Heidelberg; 1993. pp. 291-3. DOI
84. Tang, H. N.; DeVault, C.; Camayd-Muñoz, S. A.; Liu, Y. Y.; Jia, D. C. Low-loss zero-index materials. *Nano. lett.* **2021**, *21*, 914-20. DOI
85. Minkov, M.; Williamson, I. A. D.; Xiao, M.; Fan, S. Zero-index bound states in the continuum. *Phys. Rev. Lett.* **2018**, *121*, 263901. DOI
86. Monticone, F.; Doeleman, H. M.; Den, H. W.; Koenderink, A. F.; Alù, A. Trapping light in plain sight: embedded photonic eigenstates in zero-index metamaterials. *Laser. Photonics. Rev.* **2018**, *12*, 1700220. DOI
87. Zanganeh, E.; Sayanskiy, A.; Kosulnikov, S.; Kapitanova, P. Extreme metasurfaces enable targeted and protected wireless energy transfer. *Adv. Mater. Technol.* **2023**, *8*, 2202133. DOI
88. Sakotic, Z.; Krasnok, A.; Alú, A.; Jankovic, N. Topological scattering singularities and embedded eigenstates for polarization control and sensing applications. *Photon. Res.* **2021**, *9*, 1310-23. DOI
89. Liu, M.; Zhao, C.; Zeng, Y.; Chen, Y.; Zhao, C.; Qiu, C. W. Evolution and nonreciprocity of loss-induced topological phase singularity pairs. *Phys. Rev. Lett.* **2021**, *127*, 266101. DOI
90. Liu, M.; Xia, S.; Wan, W. J.; et al. Broadband mid-infrared non-reciprocal absorption using magnetized gradient epsilon-near-zero thin films. *Nat. Mater.* **2023**, *22*, 1196. DOI
91. Lio, G. E.; Ferraro, A.; Ritacco, T.; et al. Leveraging on ENZ Metamaterials to achieve 2D and 3D hyper-resolution in two-photon direct laser writing. *Adv. Mater.* **2021**, *33*, e2008644. DOI
92. Ferraro, A.; Lio, G. E.; Bruno, M. D. L.; et al. Hybrid camouflaged anticounterfeiting token in a paper substrate. *Adv. Mater. Technol.* **2023**, *8*, 2201010. DOI
93. Lio, G. E.; Ferraro, A.; Zappone, B.; et al. Unlocking optical coupling tunability in epsilon-near-zero metamaterials through liquid crystal nanocavities. *Adv. Opt. Mater.* **2024**, *12*, 2302483. DOI
94. Lio, G. E.; Ferraro, A.; Kowerdziej, R.; Govorov, A. O.; Wang, Z.; Caputo, R. Engineering fano-resonant hybrid metastructures with ultra-high sensing performances. *Adv. Opt. Mater.* **2023**, *11*, 2203123. DOI
95. Lee, D.; So, S.; Hu, G.; et al. Hyperbolic metamaterials: fusing artificial structures to natural 2D materials. *eLight* **2022**, *2*, 8. DOI

96. Álvarez-Pérez, G.; Folland, T. G.; Errea, I.; et al. Infrared permittivity of the biaxial van der waals semiconductor α-MoO_3 from near- and far-field correlative studies. *Adv. Mater.* **2020**, *32*, e1908176. DOI
97. Duan, J.; Alvarez-Pérez, G.; Lanza, C.; et al. Multiple and spectrally robust photonic magic angles in reconfigurable α-MoO_3 trilayers. *Nat. Mater.* **2023**, *22*, 867-72. DOI
98. Passler, N. C.; Ni, X.; Hu, G.; et al. Hyperbolic shear polaritons in low-symmetry crystals. *Nature* **2022**, *602*, 595-600. DOI PubMed PMC
99. Matson, J.; Wasserroth, S.; Ni, X.; et al. Controlling the propagation asymmetry of hyperbolic shear polaritons in beta-gallium oxide. *Nat. Commun.* **2023**, *14*, 5240. DOI PubMed PMC
100. Jacob, Z.; Kim, J.; Naik, G. V.; Boltasseva, A.; Narimanov, E. E.; Shalaev, V. M. Engineering photonic density of states using metamaterials. *Appl. Phys. B.* **2010**, *100*, 215-8. DOI
101. Yang, X.; Yao, J.; Rho, J.; Yin, X.; Zhang, X. Experimental realization of three-dimensional indefinite cavities at the nanoscale with anomalous scaling laws. *Nature. Photon.* **2012**, *6*, 450-4. DOI
102. High, A. A.; Devlin, R. C.; Dibos, A.; et al. Visible-frequency hyperbolic metasurface. *Nature* **2015**, *522*, 192-6. DOI
103. Yao, J.; Liu, Z.; Liu, Y.; et al. Optical negative refraction in bulk metamaterials of nanowires. *Science* **2008**, *321*, 930. DOI
104. Narimanov, E. E. Photonic hypercrystals. *Phys. Rev. X.* **2014**, *4*, 041014. DOI
105. Guan, F.; Guo, X.; Zeng, K.; et al. Overcoming losses in superlenses with synthetic waves of complex frequency. *Science* **2023**, *381*, 766-71. DOI
106. Galfsky, T.; Gu, J.; Narimanov, E. E.; Menon, V. M. Photonic hypercrystals for control of light-matter interactions. *Proc. Natl. Acad. Sci. U. S. A.* **2017**, *114*, 5125-9. DOI PubMed PMC
107. Galfsky, T.; Sun, Z.; Considine, C. R.; et al. Broadband enhancement of spontaneous emission in two-dimensional semiconductors using photonic hypercrystals. *Nano. Lett.* **2016**, *16*, 4940-5. DOI
108. Xue, C.; Ding, Y.; Jiang, H.; et al. Dispersionless gaps and cavity modes in photonic crystals containing hyperbolic metamaterials. *Phys. Rev. B.* **2016**, *93*, 125310. DOI
109. Hu, S.; Song, J.; Guo, Z.; et al. Omnidirectional nonreciprocal absorber realized by the magneto-optical hypercrystal. *Opt. Express.* **2022**, *30*, 12104-19. DOI
110. Hasan, M. Z.; Kane, C. L. *Colloquium*: Topological insulators. *Rev. Mod. Phys.* **2010**, *82*, 3045-67. DOI
111. Ozawa, T.; Price, H. M.; Amo, A.; et al. Topological photonics. *Rev. Mod. Phys.* **2019**, *91*, 015006. DOI
112. Wang, Z.; Chong, Y. D.; Joannopoulos, J. D.; Soljacic, M. Observation of unidirectional backscattering-immune topological electromagnetic states. *Nature* **2009**, *461*, 772-6. DOI
113. Khanikaev, A. B.; Mousavi, S. H.; Tse, W. K.; Kargarian, M.; MacDonald, A. H.; Shvets, G. Photonic topological insulators. *Nat. Mater.* **2013**, *12*, 233-9. DOI PubMed
114. Rechtsman, M. C.; Zeuner, J. M.; Plotnik, Y.; et al. Photonic Floquet topological insulators. *Nature* **2013**, *496*, 196-200. DOI
115. Gao, W.; Yang, B.; Lawrence, M.; Fang, F.; Béri, B.; Zhang, S. Photonic Weyl degeneracies in magnetized plasma. *Nat. Commun.* **2016**, *7*, 12435. DOI PubMed PMC
116. Liu, T.; Bai, K.; Zhang, Y.; et al. Finite barrier bound state. *Light. Sci. Appl.* **2024**, *13*, 69. DOI PubMed PMC
117. Yang, B.; Bi, Y.; Zhang, R. X.; et al. Momentum space toroidal moment in a photonic metamaterial. *Nat. Commun.* **2021**, *12*, 1784. DOI PubMed PMC
118. Wang, D.; Yang, B.; Zhang, R. Y.; et al. Straight photonic nodal lines with quadrupole berry curvature distribution and superimaging "Fermi Arcs". *Phys. Rev. Lett.* **2022**, *129*, 043602. DOI
119. Wang, D.; Jia, H.; Yang, Q.; Hu, J.; Zhang, Z. Q.; Chan, C. T. Intrinsic triple degeneracy point bounded by nodal surfaces in chiral photonic crystal. *Phys. Rev. Lett.* **2023**, *130*, 203802. DOI
120. Deng, W. M.; Chen, Z. M.; Li, M. Y.; et al. Ideal nodal rings of one-dimensional photonic crystals in the visible region. *Light. Sci. Appl.* **2022**, *11*, 134. DOI PubMed PMC
121. Chen, Z.; Jin, L.; Deng, W.; Chen, W.; Jiang, S.; Dong, J. Dual-polarization topological interface states in ridge photonic crystals. *ACS. Photonics.* **2024**, *11*, 2351-8. DOI
122. Hu, S.; Guo, Z.; Liu, W.; Chen, S.; Chen, H. Hyperbolic metamaterial empowered controllable photonic Weyl nodal line semimetals. *Nat. Commun.* **2024**, *15*, 2773. DOI PubMed PMC